SCIENTIFIC REPORTS

OPEN

SUBJECT AREAS:
MESOTHELIOMA
IRON
ONCOGENESIS
MECHANISMS OF DISEASE

Received
28 August 2012

Accepted
12 December 2012

Published
24 January 2013

Correspondence and requests for materials should be addressed to L.P. (lorella.pascolo@gmail.com)

The interaction of asbestos and iron in lung tissue revealed by synchrotron-based scanning X-ray microscopy

Lorella Pascolo[1], Alessandra Gianoncelli[2], Giulia Schneider[3], Murielle Salomé[4], Manuela Schneider[5], Carla Calligaro[6], Maya Kiskinova[2], Mauro Melato[1] & Clara Rizzardi[3]

[1]Institute for Maternal and Child Health, IRCCS Burlo Garofolo, 34137 Trieste, Italy, [2]Elettra-Sincrotrone Trieste S.C.p.a., Area Science Park, Basovizza 34149, Trieste, Italy, [3]Department of Anatomical Pathology, Department of Pathology and Forensic Medicine, University of Trieste, 34127 Trieste, Italy, [4]European Synchrotron Radiation Facility, BP 220, 38043 Grenoble Cedex 9, France, [5]Unit of Pathology, ASS n. 2 ''Isontina'' Department of Anatomical Pathology, Hospital of Monfalcone, 34074 Monfalcone, Gorizia, Italy, [6]Servizio Diagnostica Veterinaria, University of Udine, 33100 Udine, Italy.

Asbestos is a potent carcinogen associated with malignant mesothelioma and lung cancer but its carcinogenic mechanisms are still poorly understood. Asbestos toxicity is ascribed to its particular physico-chemical characteristics, and one of them is the presence of and ability to adsorb iron, which may cause an alteration of iron homeostasis in the tissue. This observational study reports a combination of advanced synchrotron-based X-ray imaging and micro-spectroscopic methods that provide correlative morphological and chemical information for shedding light on iron mobilization features during asbestos permanence in lung tissue. The results show that the processes responsible for the unusual distribution of iron at different stages of interaction with the fibres also involve calcium, phosphorus and magnesium. It has been confirmed that the dominant iron form present in asbestos bodies is ferritin, while the concurrent presence of haematite suggests alteration of iron chemistry during asbestos body permanence.

Asbestos is a fibrous silicate with particular physical/chemical properties and tensile strength that makes it an ideal material for various construction and covering purposes. For this reason it was widely used for more than 100 years and is currently still used in some countries, despite the alarming reports about its toxicity and possible carcinogenicity[1]. Asbestos exposure has clearly been associated with development of pulmonary diseases including bronchogenic carcinoma, mesothelioma, pleural plaque and asbestosis (pulmonary fibrosis due to asbestos exposure). A very recent report of the International Agency for Research on Cancer (IARC) classifies all types of asbestos as carcinogenic to humans with sufficient evidence for different types of cancers[2].

While asbestos toxicity is undeniable, the exact pathogenic mechanisms and the precise co-factors by which asbestos fibres trigger pulmonary toxicity and neoplastic transformation have not been fully understood. Many groups are continuously reconsidering and researching the mechanisms relevant to asbestos's pathogenicity. These include generation of Fe derived free radicals and reactive nitrogen species, release of cytokines, as well as induced genotoxicity and alteration of immune responses. In addition, ionizing radiation and simian virus 40 (SV40) may play some roles specifically in the induction of mesothelioma[3–7].

Following decades of fibre toxicology studies, asbestos toxicity is considered a consequence of some characteristic physico-chemical properties of the material[8–10]. For fibres in general, the pathogenicity is described within a toxicology structure-activity paradigm, the main determinants being fibre length, diameter and bio-persistence[8]. For asbestos, specific chemical composition of the materials and surface properties should also to be considered as potentially affecting bio-persistence and thus carcinogenic effects[10].

The presence of transition metals in the fibres and/or the ability of the fibres to adsorb and accumulate them are the first mechanisms suggested for explaining the toxic and particularly carcinogenic effects of asbestos[11–13]. The presence of iron in the fibres (which may contain up to 30% of Fe w/w) and more importantly the intrinsic ability to attract it from the surrounding environment seems to be also a key factor for asbestos toxicity and for the formation in the lung of the asbestos bodies that are the hallmarks of asbestos exposure[5,14].

The formation of an asbestos body is an intriguing phenomenon that results in the deposition of endogenous iron, iron containing proteins (as ferritin), mucopolysaccharides and other material on bio-persistent fibres in the

lungs. On one hand, it is believed that the shell that is formed isolates the fibre from the tissue and reduces its damaging effect. On the other hand, the locally altered homeostasis of iron produced by the reaction to asbestos fibres and body formation, together with the presence of a potentially reversible iron reservoir constituted by the iron-containing protein aggregates, is considered as responsible for an increase of iron mediated ROS production. This may trigger asbestos related diseases, with potential DNA damage and apoptosis resistance[5,14,15].

Not all asbestos fibres found in lung are coated (variable percentages of free fibres are observed by different techniques), however correlation between asbestos related diseases and the relative abundance of coated to uncoated fibres has not been demonstrated yet. Similarly, lung tissue burdens of asbestos fibres have long been used as an index of exposure, but the studies have not established correlations between this index and cancer development[16,17].

It is interesting that according to the most recent views, the central role of iron in asbestos toxicity and related diseases pathogenesis is consistent with a more general picture of a steadily growing number of diseases characterized by imbalance of the iron metabolism in cells and tissues. Concerning this issue, the recent reviews by D. Kell[18,19] analyse the wide but dispersed literature via a systems biology approach, and indicate that iron that is weakly complexed boosts many biochemical processes leading to a large variety of apparently unrelated diseases. Among the most prominent examples are Alzheimer's and Parkinson's diseases, metabolic syndrome, diabetes, atherosclerosis and even cancer. Understanding the mechanisms of iron participation in the aetiology of these pathologies may lead to novel therapeutic targets.

Iron in living cells is a trace element and has a crucial role, acting as a redox component of fundamental enzymes and proteins. However, the same divalent character of iron that plays an important biological role, may cause toxicity by sustaining oxidative stress conditions. Due to the presence of high-affinity iron binding and storage proteins, the actual toxicity of iron is restricted to the so called "labile iron pool". Chronic increase of such 'free' iron forms are associated with pathological conditions and possible complex homeostasis unbalance for this element in cells and tissues, relevant to asbestos toxicity and related diseases[18–20].

It is known that airway epithelial cells and alveolar macrophages in lung have an active iron metabolism. The airway epithelial cells, acting as the first line defence against environmental insults, including asbestos, may be efficient in reducing non-transferrin-bound iron, converting it to less toxic protein-bound iron[21,22]. However, the major lung defence is performed by one class of macrophages (alveolar macrophages) that, interacting and responding to various stresses, are capable of iron scavenging too, protecting lung tissue against oxidative damage[23–25]. These macrophages are also involved in the pathogenesis of asbestosis and cancer[5,25,26]. During inflammation, iron efflux from alveolar macrophages may be induced via several mechanisms. The paths involved in the overall iron mobilization and utilization by alveolar macrophages as well as epithelial cells are largely unknown. One of the reasons is the limited performance of specific conventional histological staining procedures used for such investigations.

Little is also known about the cellular structures that are involved in transient storing of iron and the real fate and chemical reactivity of metal ions under normal and pathological conditions.

An important initial step towards unravelling all these issues is the identification and localization of the metal in native physiological environments in tissues and cells. In this respect synchrotron-based X-ray microscopy approaches are becoming very desirable tools providing correlated morphology and chemical information of the specimen. The combination of X-ray imaging with X-ray Fluorescence microscopy (μ-XRF) allows monitoring of the distribution of elements in tissue samples without artefacts[27,28], as demonstrated in our recent study of asbestos bodies[29]. In this first study we also revealed the contribution of magnesium to the asbestos body formation, which appears to be related to the presence of iron as well.

The present study further explores the chemistry of tissue reaction to the presence of asbestos by primarily using a medium energy XRF microscopy set-up which allowed us to investigate and resolve at high spatial resolution the presence of iron and other biologically relevant elements in the lungs of asbestos exposed patients. Correlative analyses for light elements were performed on the same samples under a low energy X-ray microscopy set-up. In addition, we report X-ray absorption near edge spectroscopy (XANES) analyses, which for the first time show the speciation of iron in the asbestos bodies.

Results

Histological analyses and iron detection by Perls' staining. The enrolled patients had medium to high content of asbestos bodies in their pulmonary parenchyma according to asbestos bodies counts performed on digested lung tissue (as reported in Table 1). Despite the differences in the estimated fibre content or the presence of concurrent malignancies (cancer or mesothelioma), we selected for the present analyses comparable lung tissue sections (avoiding malignancies), having the specific histological features of asbestosis and clearly recognizable asbestos bodies. In the selected tissue slices (at least 2 per patient, more than 30 in total), the examined asbestos bodies were of various dimensions and shapes. Some of them were isolated or grouped inside dense interstitial fibrosis deposition material, others were surrounded and/or interacting with macrophages and giant cells. The histological appearance of asbestos bodies are in line with those reported by many other authors[30,31] and no apparent differences were observed between the samples from mesothelioma patients and the others.

Panels (a) and (b) in Figure 1 show the appearances of some isolated asbestos bodies and examples of fibres phagocyted by alveolar macrophages, as obtained by histological routine analyses with hematoxyl in and eosin staining.

In order to investigate the presence and distribution of non-heme Fe (ferric) in the tissues, Perls' staining was performed on the different sample tissues, and in all analysed tissues most of the asbestos bodies and also the frequent sideromacrophages appeared positive (blue colour). In Figure 1 (Panel c) iron staining is revealed inside macrophages exhibiting phagocytosis of fibres, while the dye does not colour free fibres (panel d), suggesting that the iron in the fibre does not react with this dye. The Perls' positive staining in the tissues was maximal in the regions with high levels of inflammation.

The asbestos containing regions selected for X-ray microscopy studies had increased presence of macrophages and lymphocytes, in accordance with the inflammatory conditions of the patients.

Elemental mapping with XRF microscopy. In order to access both the lateral distribution of light and some heavy elements in the tissue samples, we performed the experiments using soft X-rays (up to 2200 eV) and hard X-rays (up to 7.3 keV). In particular the hard X-rays were required for mapping Ca, S and P, whereas soft X-ray microscopy provided higher quality absorption and phase contrast images.

During two different beamtimes at ID21 (ESRF) and four at TwinMic (Elettra) we analysed about 20 tissue slices, obtaining elemental maps for about thirty asbestos bodies. Although in each sample different types of fibres and asbestos bodies can be present we did not find characteristic features related to the specific patient diagnosis. In particular we did not find any chemical difference in the maps from the asbestos bodies and the surrounding tissue in samples obtained from mesothelioma patients. Here we report selected images that show the characteristic chemical content in the samples, containing typical asbestos bodies.

Table 1 | Patient description

Patients	Age	Sex	Occupation history	Asbestos body count	Pathological Diagnosis
A1	75	M	Naval shipyard worker (Monfalcone)	1,209,375	Asbestosis (grade >2)
A2	77	M	Naval shipyard worker (Monfalcone)	25,600	Asbestosis (grade 2)
A3	93	M	Naval shipyard worker (Monfalcone)	1,400	Asbestosis (grade 2)
A4	74	M	Naval shipyard worker (Monfalcone)	2,700	Asbestosis (grade 2)
A5	83	M	Naval shipyard worker (Monfalcone)	557,685	Asbestosis (grade 2), peritoneal and pericardial mesotelioma
C1	71	M	Naval shipyard worker (Monfalcone)	108,000	Asbestosis (grade 2), lung cancer
M1	81	M	Naval shipyard worker (Monfalcone)	950,000	Epithelioid mesothelioma, asbestosis (grade >2)
M2	70	M	Naval shipyard worker (Monfalcone)	51,635	Epithelioid mesothelioma, asbestosis (grade 2)
M3	87	F	Naval shipyard worker (Monfalcone)	1,140	Epithelioid mesothelioma, asbestosis (grade 1)
M4	85	M	Naval shipyard worker (Monfalcone)	22,453	Biphasic mesothelioma, asbestosis(garde 2)

Figure 2 reports the light microscopy image (a), X-ray absorption image (b) and the corresponding XRF elemental maps of a tissue section from a patient with asbestosis (A1 from Table 1). The asbestos body is simply identified by light microscopy (panel a), while the X-ray absorption image in panel (b) allows better definition of the features of the body. The XRF elemental maps clearly distinguish the original silicate fibre (~60 μm length) (Si map), which is the core of the segmented body that has developed around it. The coating is best represented by the P and Fe maps. Due to the extremely high abundance of Fe in the asbestos coating, the Fe signal is reported also on a logarithmic scale in order to highlight its presence in the surroundings as well. In fact, the Fe log map clearly shows accumulation of Fe in the vicinity of the asbestos bodies both as diffuse signal and as bright spots organised in a manner resembling intracellular vesicles or siderosomes. The panel above the Fe map shows the intensity profiles taken across the dashed lines in the Fe log image, where one can see the dimensions and relative Fe content in the body and in the region up to ~15–20 μm around the body, where the bright features are believed to be vesicles. In fact, there is fair correspondence between the lateral organization of these small bright features in the Fe log map and the features that can be attributed to cells in the P and S maps. Sulfur seems to be a good marker of cell substance and possibly useful to delineate cytoplasmic borders when compared to the phosphorus signal. By close inspection of the distribution profile and intensity levels, it seems that one can identify in the P map the cell nuclei where the content of this element is high. When merging the P, Si and Fe maps (P-Fe-Si) or P, Si and S maps (P-Si-S), it appears that both the majority of iron diffuse signal and the vesicular spots, are mainly related to the presence of macrophage-like cells, and especially the distribution of sulfur and phosphorus located in the proximity of the asbestos body supports this interpretation. The calcium distribution (Ca) seems to correlate with cell and tissue architecture but it is much more abundant in the coating of the asbestos body.

Figure 3 shows the results of a tissue section from another patient with asbestosis (A3 from Table 1), containing uncoated fibres or fibres with a very thin coat. This fibre types are not easily visible and are difficult to detect using routine and conventional

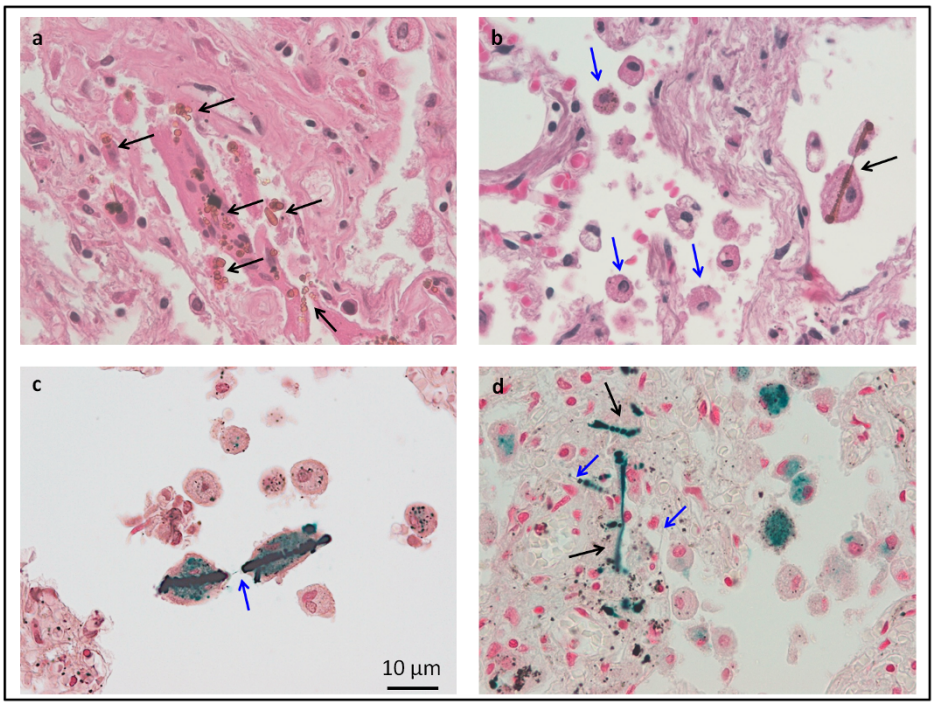

Figure 1 | Histological examination of human lung tissue with asbestos bodies. Panel (a) and (b) are microphotographs from the histological sections used for the study, stained by hematoxilin and eosin. Diffuse fibrosis and asbestos bodies (black arrows) are evident. In panel (b) there are sparse macrophages (blue arrows) and an asbestos fibre is phagocytated by two macrophages (black arrow). Panel (c) and (d) show tissue sections colored with Perls' staining and positive staining of asbestos bodies (black arrows). Uncoated fibre parts are not stained (blue arrows). In (a), (b), (d) magnification is 40×, while in (c) is 60×.

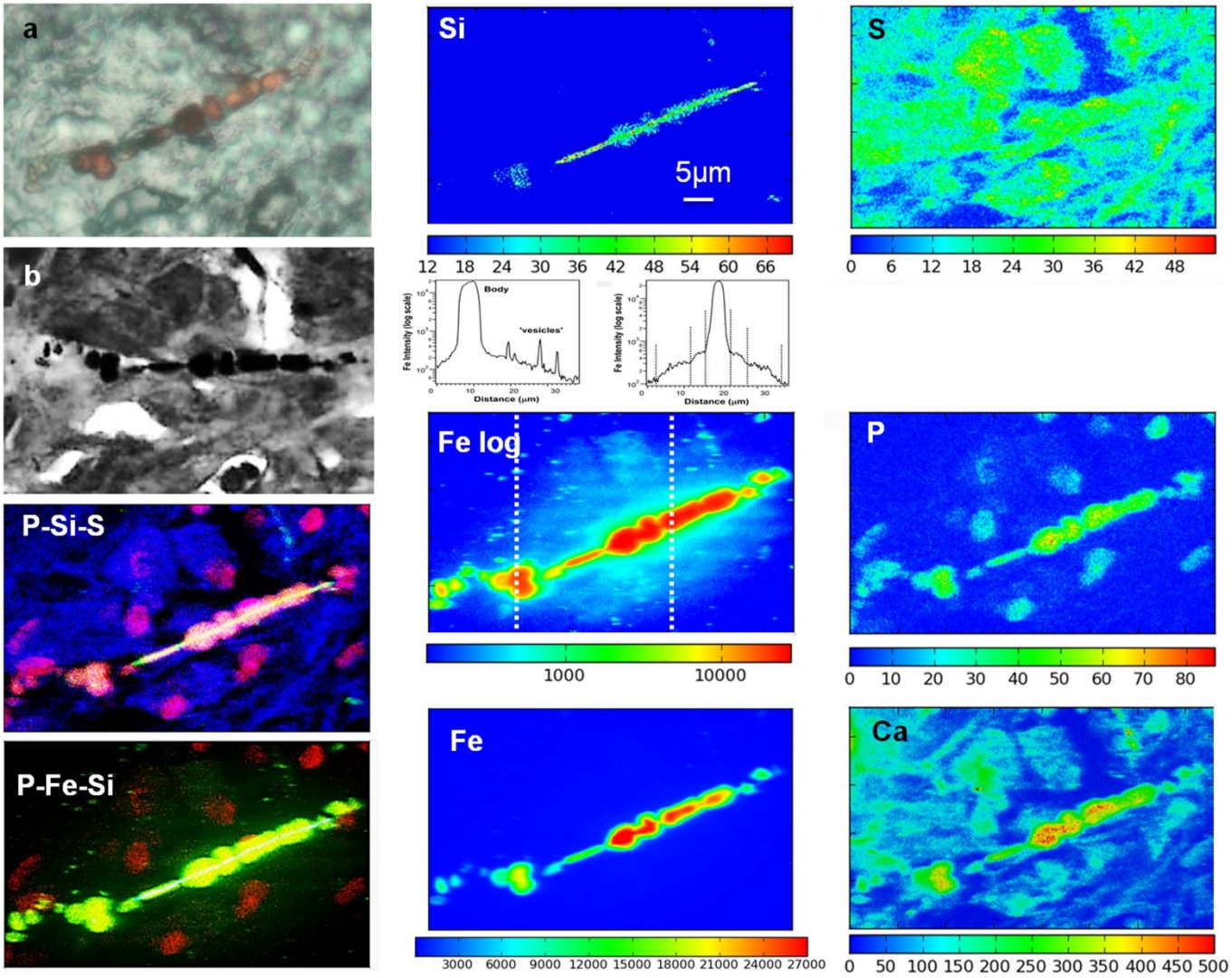

Figure 2 | µXRF and X-ray microscopy of tissue section containing asbestos. Visible light image of the unstained tissue section (a), 80 × 50 µm² X-ray microscopy absorption image (b) and the corresponding Si, Ca, P, S, Fe and co-localisation (P-Si-S and P-Fe-Si) XRF maps (62 × 38 µm²) showing the distribution of different elements in a tissue section containing asbestos. The panels above the Fe map illustrate the Fe intensity profiles measured across lines indicated in the image. The absorption image was measured at the TwinMic beam line with photon energy 0.9 keV, whereas the XRF maps were acquired at ID21 beamline at 7.3 keV.

microscopy. Their presence in tissues is mainly monitored during asbestos body extraction procedures or using TEM microscopy. Both the thin fibres (not visible under light microscopy) and the thin bodies are clearly distinguished in the soft X-ray absorption (a) and phase contrast (b) images. The Fe map (logarithmic scale) also reveals many fibres of various dimensions that apparently contain the element or, very likely, have adsorbed it forming a very thin coating. In addition, there is a detectable increase of iron concentration around the fibres and the bodies, where some brighter features suggest also the presence of small vesicles or aggregates. In this sample there is an abundance of phosphorus in the asbestos bodies, similarly to Figure 2, but the distributions of sulfur and phosphorus (panels S and P) do not allow recognition of specific cell structures. The calcium distribution (Ca) shows high concentrations only in the formed asbestos bodies, while apparently there is no Ca increase around the thin 'naked' fibres. Further complementary XRF investigations highlight the distribution of silicon and magnesium in some selected regions (areas C and D, panel a) of the map (panels Mg_1, Si_1, Mg_2, Si_2 respectively). The Mg_1 map confirms the presence of magnesium inside or on top of the fibres (panels Si_1 and area C), suggesting aggregation of a thin layer similar to but less uniform than that of iron (Fe_1). The Si_2 map clearly shows the asbestos fibres (not visible in the absorption image of Panel d); some of them are not visible in the Fe map, which is in accordance with the different Fe content in different types of asbestos. Magnesium (Mg_2) is mostly concentrated in the strongly coated segments, its distribution being similar but not identical to that of Fe.

Figure 4 illustrates different steps of iron aggregation around the original fibre of an asbestos body present in the lung tissue of a patient with asbestosis and mesothelioma (M1 in Table 1). The tissue response to the low iron containing asbestos fibre (panels Si and Fe) is the formation of a segmented asbestos body with high Fe, Ca and Mg content. Both calcium and magnesium appear marginally present in the original fibre. More detailed information about the presence and relative concentrations of the elements in different locations is obtained from the XRF spectra measured in selected spots, indicated in Panel (a). The relative intensities of Si, Mg, Fe and O indicate that points A and B represent the composition of an almost bare fibre, point C and D possibly early stages of body formation or simply a very thin coating and point E the fully developed body segments. It should be noted that the segmented structure assumes that the growth of coating bodies is much faster in specific

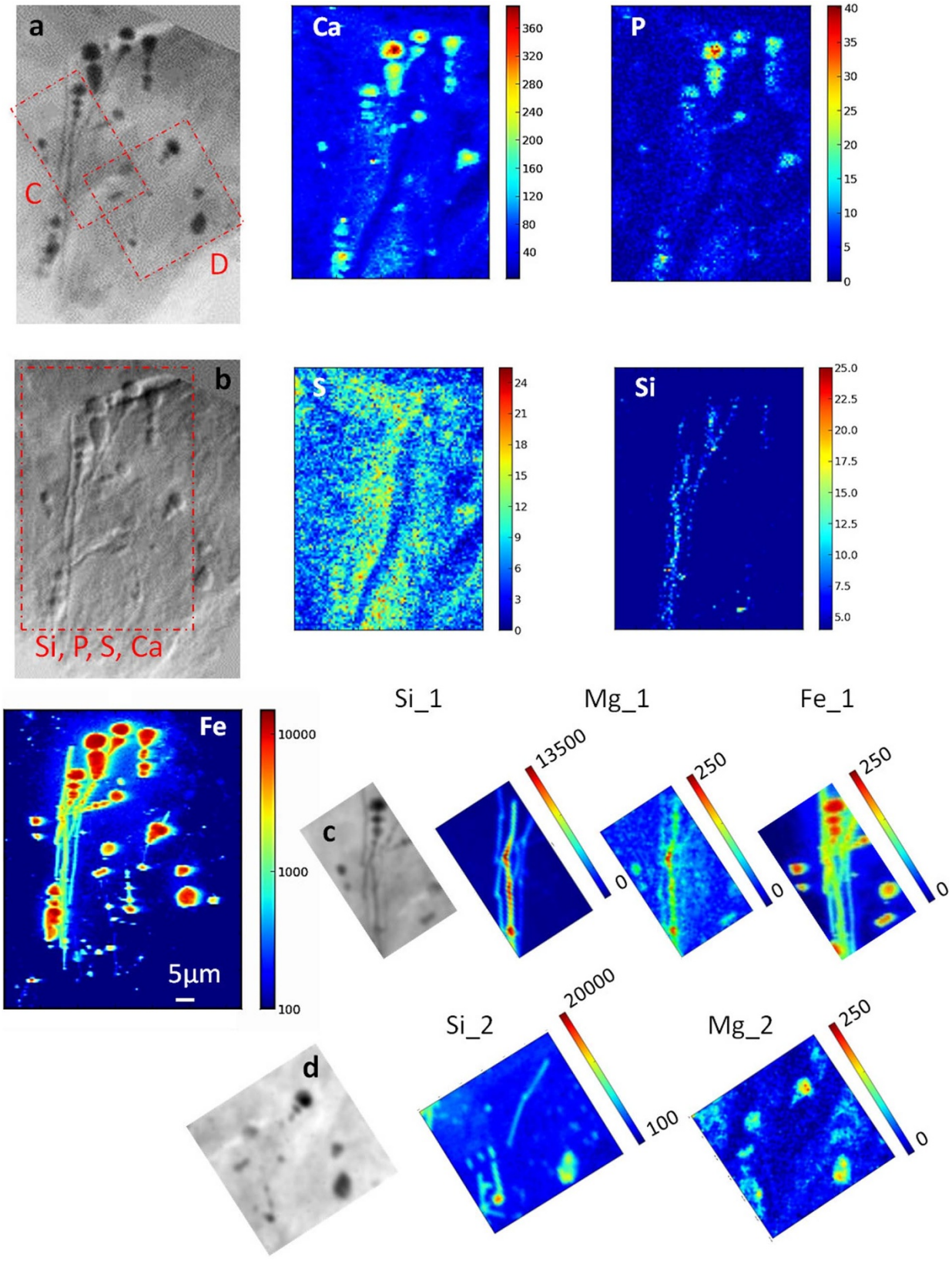

Figure 3 | µXRF and X-ray microscopy of tissue section containing uncoated asbestos fibres. 65 × 80 µm² X-ray microscopy absorption (a) and phase contrast (b) images and the corresponding XRF Ca, P, S, Si (45 × 60 µm²) and Fe (65 × 80 µm²) maps of a tissue section containing asbestos. These XRF maps were acquired at ID21 at 7.3 keV. The parallax mismatch between the images collected at the TwinMic beamline (absorption, phase contrast) and the ones acquired at the ID21 beamline (Fe, Ca and S) is due to the different geometrical set up of the two systems. In the TwinMic microscope the incoming beam hits the sample perpendicularly while at the ID21 beamline the sample is tilted of 30 degrees with respect to the incident X-ray beam. The 18 × 30 µm² XRF maps Si_1 and Mg_1 and Fe_1 corresponding to area C (panel c), indicated in panel (a), and 30 × 30 µm² Si_2 and Mg_2 corresponding to area D (panel d) were acquired with 1.9 keV at TwinMic.

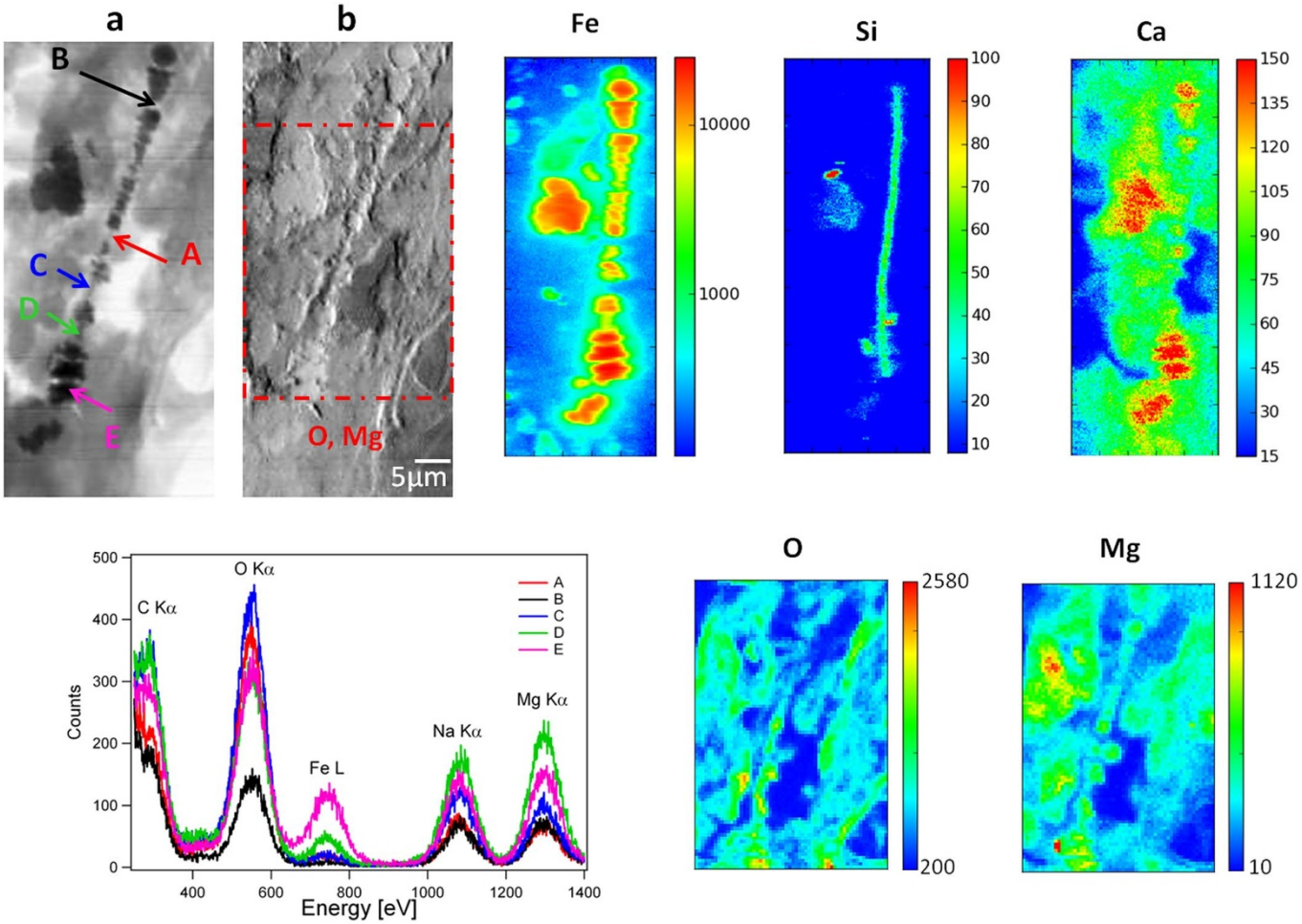

Figure 4 | Ferruginous body of an iron free asbestos fibre. 30 × 65 µm² X-ray microscopy absorption (a) and phase contrast (b) images and the corresponding XRF Fe, Si, Ca (26 × 68 µm²) O and Mg (30 × 45 µm²) XRF maps of a ferruginous body developed on an iron-free asbestos fibre. The XRF spectra panel outlines the relative intensities of O, Fe and Mg in the spots indicated in panel A. The X-ray images, Mg and O maps and the XRF spectra were acquired with 1.5 keV photon energy, whereas the Fe, Si and Ca were taken at 7.3 keV. As in Figure 3, parallax mismatch must be considered between images collected at the TwinMic beamline (absorption, phase contrast, O and Mg maps) and those at the ID21.

fibre locations, which should have some structural and/or composition characteristics resulting in enhanced local reactivity with the tissue. An interesting result is that the thin coated fibre segments (point D) have a high magnesium content, despite modest iron aggregation, similarly to the poorly coated fibres in Figure 3. The O signal is localised together with Fe, Mg and Si, indicating that these elements are present in oxide forms.

Figure 5 (patient A5 in table 1) reports a case of an asbestos fibre, apparently phagocyted by two macrophages as revealed by X-ray microscopy and XRF elemental mapping. This is an example of incomplete phagocytosis, where two cells are unable to isolate completely the fibre. The phase contrast (panel b) and absorption (panel a) images show a broken fibre with the classical dumbbell-shaped high absorbing extremities. The exact morphology of the original fibre is revealed by the Si map (panel Si). The dark features in the absorption image are due mainly to the presence of strongly absorbing iron (panel Fe), while brighter features outline the cellular borders. The iron intensity is reported both on linear and logarithmic scales to illustrate better the quantitative ranges. The linear scale image reveals a very high iron concentration at the extremities of the body, an apparently substantial concentration in the original fibre and a continuous, multilayer aggregation around it. As better seen with the logarithmic scale (panel Fe log), iron appears abundantly distributed just above the body, clearly delineating cellular contents (diffuse signal) and some intense intracellular or extracellular vesicle-like structures (1–5 µm). Sulfur and phosphorus maps allow us to distinguish the dimensions and the poly nuclei of the macrophages, during phagocytosis as well as other tissue structures. From these results, while the presence of iron cannot be assigned with certainty to the original fibre, calcium and magnesium appear almost absent in the fibre. Both calcium and magnesium tend to localize together with phosphate in the asbestos coating, but their distributions are not identical, e.g. magnesium is more abundant in the extracellular segments. It is also interesting that the phosphorus intensity in the coating (panel P) is comparable with that of the cell nuclei, and even much higher at the extremities suggesting the maximal calcification there.

In Figure 6 we report an example of relative quantitative distribution in some selected areas of the bodies reported in Figures 2, 4 and 5. Due to the difficulty of preparing suitable reference standards for absolute quantification in samples with inhomogeneous density (strong absorbing asbestos bodies in organic matter) we compared the Fe, P and Ca content of the selected regions (1 µm² areas) with that of a blood vessel section in an asbestos free area. The estimations in the table of Figure 6 are reported in terms of multiples of signal increase *vs.* the average content of four blood vessel areas (1 µm² each) with a maximal iron content (see panel Fe in figure S1). The semiquantitative results were obtained by using the Fundamental Parameter Method provided by PyMCA software[32]. This approach allowed us to highlight the extremely high content of iron on asbestos

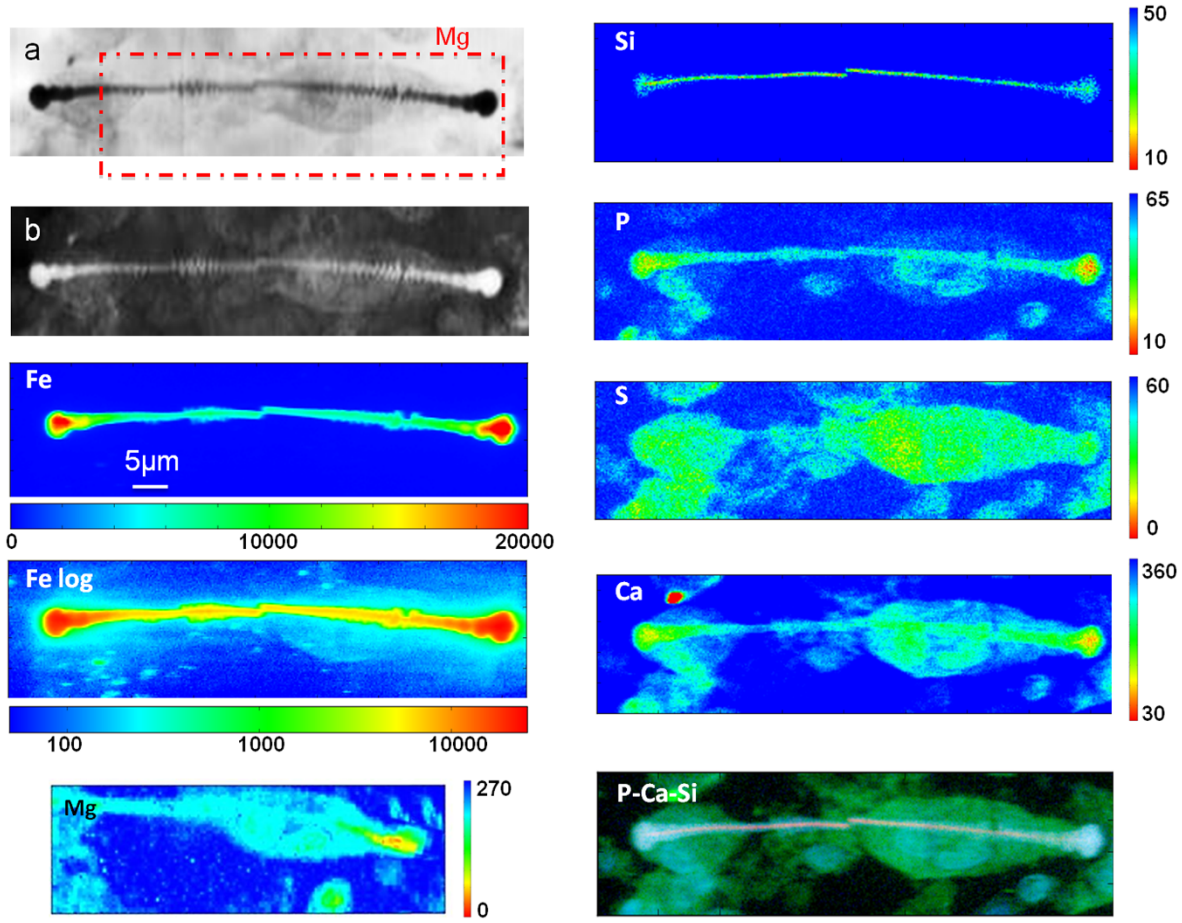

Figure 5 | Tissue with phagocytated asbestos fibre. 80 × 20 μm² X-ray microscopy absorption (a) and phase contrast (b) images and the corresponding XRF Fe, Si, P, S Ca (84 × 22 μm²) and Mg (62 × 20 μm²) XRF maps of a tissue with phagocytated asbestos fibre. Fe log is displayed using a logarithmic scale and Fe using a linear scale. The P-Ca-Si co-localization is illustrated below right. All images were acquired at 7.3 keV except the Mg map which was acquired at 1.5 keV. As in previous figures, parallax mismatch must be considered between images acquired at the TwinMic beamline (absorption, phase contrast and Mg map) and those at the ID21 beamline.

bodies (up to 400 times that of the vessel) accompanied by a sensible increase of P and Ca as well. In addition, in close proximity of the bodies and surrounding structures we detected iron values all higher than those in the vessel.

X-ray absorption near edge spectroscopy (XANES). The oxidation state of Fe provides important information on the processes involved in the asbestos body formation, and has been obtained from Fe K-edge XANES, measured in selected ~1 μm² spots from the Fe maps. Although this technique allows elemental oxidation states to be probed with high spatial resolution, in the case of asbestos bodies and tissues, only sufficiently wide and flat bodies can be successfully analysed, at the limit of the micro-beam stability during energy scans. The signal was not sufficient to obtain reliable microspot spectra from the regions with low Fe content surrounding the asbestos body. The measured spectra were deconvoluted using spectral standards for ferritin, haematite, crocidolite fibres, magnetite, metallic iron and fayalite. The representative Fe K-edge spectrum shown in Figure 7 is apparently dominated by features characteristic for ferritin (ferrihydrite containing protein) and smaller amounts of haematite and crocidolite. This confirms that most of the iron detected around asbestos fibres (coating and ferruginous bodies) is compatible with the presence of ferritin and the Fe^{3+} oxidation state of iron. The micro-XANES spectra collected from different asbestos bodies in different samples exhibit an average composition of 71% ferritin (ferrihydrite), 16% haematite, 12% crocidolite and 1% metallic iron. Other forms of iron were not detected in the measured spectra.

Discussion

For the present work we selected ten patients out of a cohort of 200 subjects exposed to asbestos (from the same shipyard area) in order to provide an appropriate representative sampling for studying the chemistry of asbestos body formation and fibre effects in the lung. The data presented show for the first time different aspects of the iron concentration, distribution and speciation in diseased human lungs after asbestos exposure, that cannot be observed using conventional techniques[5,33] (Figure 1). Due to the unique sensitivity of synchrotron μ−XRF we obtained elemental maps which clearly demonstrate that long-lasting asbestos fibres and bodies cause large mobilization of iron into the surrounding cells (mainly alveolar macrophages) and in the tissue, partially consequent to continuous iron adsorption onto the fibres and/or asbestos body degradation and metal release.

As demonstrated by Figures 2, 4 and 5, the XRF elemental mapping allows clear identification of asbestos fibre and asbestos body shape, determined from Si and Fe distributions respectively, while phosphorus and sulfur signals can be used to recognise cell morphologies in unstained histological sections. Indeed, the S and P distributions measured by XRF have already been used as indicators of cellular components, in cell samples[34] and, with a similar technique (PIXE) but at lower lateral resolution, also in human lung tissue sections[35]. In our study the spatial resolution provided, confirms that

	Zone1	Zone2	Zone3	Zone4	Zone5	Zone6	Zone7	Zone8	Zone9	Zone10	Zone11
Fe	400x	75x	2x	240x	25x	8x	60x	5x	325x	15x	4x
Ca	24x	7x	10x	13x	8x	7x	9x	4x	30x	7x	8x
P	140	45x	50x	190x	100x	100x	145x	50x	150x	16x	13x

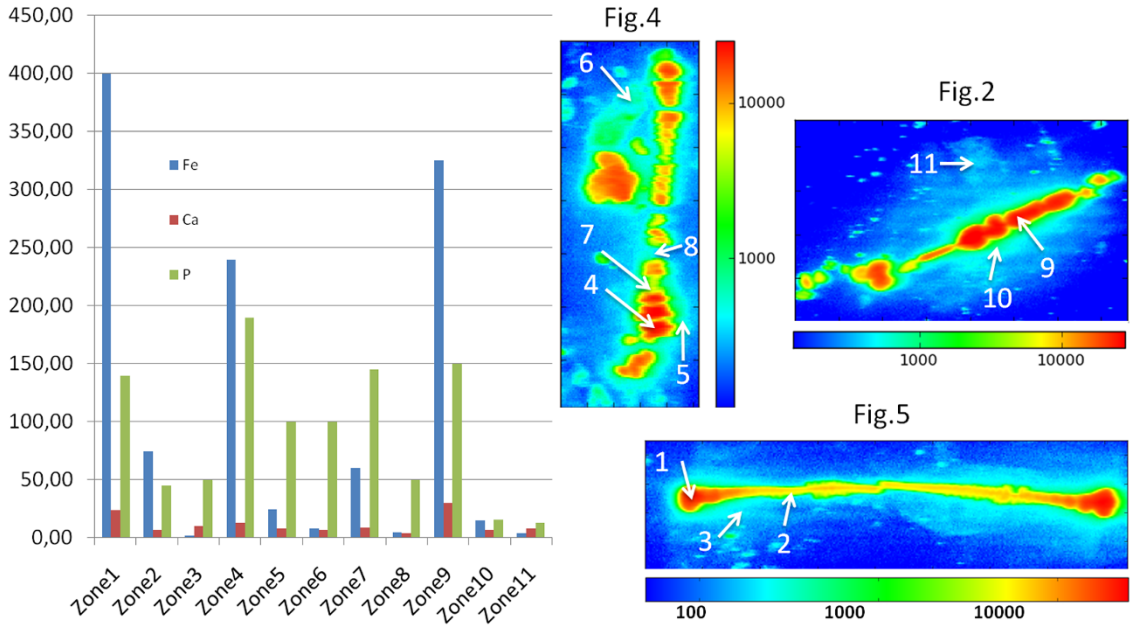

Figure 6 | XRF semi-quantitative analyses of Fe, P and Ca content in asbestos bodies and tissues. The table reports the comparative evaluation of Fe, P and Ca in the specific areas indicated in the Fe maps of Figure 2, 4 and 5 (right bottom panels). The values are indicated in terms of multiples of signal increase *vs.* the average content of four blood vessel areas (all normalized to 1 μm^2) marked in figure S1, panel Fe. The bottom left graph shows the relative amount of Fe, Ca and P in the ten selected areas (as reported in the top table).

probing the distribution of these two elements can be employed for investigating in detail the cellular mechanism in unstained tissues. In our study we successfully traced the presence of iron in some alveolar macrophages, in the vicinity of asbestos bodies and the fibre phagocyting cells (Figures 2 and 5). While the results in Figure 5 clearly show the phagocytosis of a fibre, with alteration of iron concentration in the cells, Figure 2 suggests that the well developed asbestos bodies are not necessarily inert structures but continue to inflame the tissue (many macrophages present). Indeed, previous studies[15,20] have also suggested that asbestos causes an increase of ferritin in alveolar macrophages and in the tissue, but here we provide substantial qualitative and quantitative information to help understand the complex body formation mechanism. Figure 2 reveals the presence of micro- and nano-aggregates (vesicles) with relatively high Fe content in the proximity of the asbestos body. From the measured Fe signal one can estimate the relative Fe content in the body, vesicles and the near-by regions as being up to 1000 times higher than the Fe content in non-affected tissue. A more quantitative comparison is available in Figure 6 where the relative Fe content is shown for different areas in the samples. The higher Fe content in the zone near the asbestos can be ascribed to two possible scenarios: furthering of processes that result in an increased deposit of Fe-containing species around the body or release of some iron species from the body and fibre due to possible degradation processes. In fact, deposition of Fe-containing species around the original fibres is evidently a multistep phenomenon. Figure 4 indicates that probably the particular physico-chemical characteristics of original asbestos fibres determine whether thin or thick deposits will be formed. In fact, even the apparent 'uncoated' fibres (Figure 3) alter iron homeostasis of the lung tissue and most likely they are covered with very thin deposits. The observation of nanoformations and microaggregates is an intriguing result for such a scenario, inviting further investigations of and speculations on the biological role of such iron structures. As already supposed and reported in some studies[33,36], other chemical elements participate

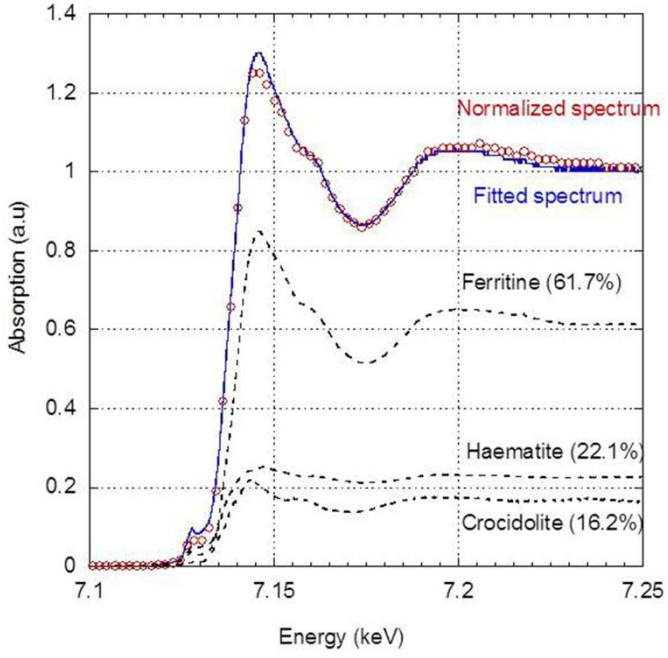

Figure 7 | Micro-XANES analyses on asbestos bodies. An example of a deconvoluted micro-XANES spectrum of an asbestos body measured with a microprobe of 1 μm^2.

to the formation of asbestos bodies as well. The high amount of phosphorus, calcium and magnesium in the fibre casing, compared to their content in the cells, is evidenced by the corresponding XRF maps, which suggests that calcification is occurring along with iron (ferritin) deposition. Calcification seems to be a consequence of phagocytosis (Figure 5), while calcium looks weakly attracted by the thin coated fibre regions (Figure 3 and 4). We previously demonstrated the presence of magnesium in asbestos bodies, suggesting that Mg plays a role in determining irreversible calcifications[29]. Interestingly here we found that magnesium is also present around the fibres and segments with very thin coatings, possibly interacting with iron species and their transporters. In our opinion the first steps of interaction of the asbestos fibres with tissues involve attraction of iron-containing species combined or followed by magnesium aggregation, in fair agreement with some featured results in Figure 4 (points C and D) and the results for the fibres with very thin deposits in Figure 3. In the following stages the bio-mineralization process continues possibly inside the macrophages, involving ferritin together with phosphate, calcium and magnesium.

Undoubtedly, further details about the chemical nature of iron containing bodies and aggregates will contribute to understanding their pathogenic significance (as for aggregates in neurodegenerative diseases)[37] and, in addition, to potentially discriminate the fate of iron containing fibres from iron-free asbestos. In this respect, the XANES analyses on a significant number of asbestos bodies from different patients allowed us to detect and quantify the relative concentration of crocidolite material in some asbestos bodies, demonstrating the potential of XANES in investigating asbestos and its effects in tissues and for forensic research as well. More importantly, our data indicate that the iron in the asbestos bodies is prevalently trivalent (Fe^{3+}) and, as expected, corresponds to ferritin standards, thus being in the mineral form of ferrihydrite. While revealing only a minimal concentration of metallic iron, the novelty here resides in the detection of a significant and variable percentage of haematite in the bodies. In fact, a recent work[38] has already reported the detection of haematite in asbestos bodies by Raman spectroscopy, however explaining the result as a mere artefact and the outcome of irradiation and thermal transformation of asbestos body ferritin. Since such beam-dependent transformation is unlikely in our study, we suppose that the detected haematite is a result of ferrihydrite (from ferritin) transformation occurring during the long residence time in the asbestos coating. This hypothesis is in agreement with the recent detection of haematite in other diseases, characterized by ferritin and hemosiderin anomalous accumulation[39,40] and with the recent observations of structural and magnetic changes during the transformation of ferrihydrite into haematite produced by aging[41].

Methods

Patients, histological sample preparation, asbestos body count. From a cohort of more than 200 former shipyard workers exposed to asbestos and died for asbestos-related diseases, autopsied at the Unit of Pathology of the St. Polo Hospital of Monfalcone (Italy) we selected ten patients, considered representative of the group according to the following characteristics: work place and nature, exposure to asbestos, type of disease clinically monitored and verified by autoptic examination. The demographic description of the ten patients is reported in Table 1.

The study was approved by the ethics boards of the Medical Faculty of the University of Trieste and of the Monfalcone Hospital (Italy). Human samples consisted of tissues discarded after forensic autopsy, and were retrieved with the approval of the institution. Samples were anonymous at the date of the study, namely, while clinical diagnosis was recorded, it was impossible to retrieve personal information of the patients. Histological examination of the samples and histological diagnosis of asbestos-related disease, namely asbestosis, lung cancer or mesothelioma was carried out at the St. Polo Hospital of Monfalcone by some of the authors, who are pathologists experienced in asbestos-related pathology. Histological diagnosis and grading of asbestosis was established according to the Roggli-Pratt modification of the CAP-NIOSH system as recommended by the Helsinki criteria[42], which require the identification of diffuse interstitial fibrosis plus the presence of either two or more asbestos bodies in tissue with a section area of 1 cm^2 or a count of uncoated asbestos fibres falling into the range recorded for asbestosis by the laboratory. All selected patients were affected by pulmonary asbestosis, one had also lung cancer, while four had also pleural mesothelioma (Table 1). The asbestos body identification was performed by light microscopy (Leica Microsystems, Germany) on 3 μm thick sections from paraffin-embedded samples of non-neoplastic lung tissue both unstained and stained with hematoxylin and eosin according to the standard protocol. For each patient at least two sections positive for the presence of asbestos were considered for XRF and Perls' analyses. For X-ray imaging and XRF analyses, 5 μm thick sections were cut from the selected tissue regions, mounted on ultralene foils (4 μm thick) and air-dried, as previously described[29].

The extraction and count of the asbestos bodies were performed using a routine method[43] with some modifications as previously reported[29]. Briefly, for each preparation two samples (1–2 g) were excised from the basal side of the right lung lobe, avoiding tumoral lesions, and were rapidly fixed in formalin 10%. One sample was used for asbestos extraction and the other one for calculating the wet on dry weight ratio after a dehydrating procedure at 40°C for 24 hrs. For the extraction, the sample was ground, placed in sodium hypochlorite (20%) and left to digest at 40°C for 24 hrs. The sediment was recovered, re-suspended in chloroform and ethanol (50%) (1 : 1) and centrifuged at 800 rpm for 10 min. The supernatant liquid was aspirated, leaving about 1 ml of liquid covering the pellet that was then re-suspended with ethanol and subsequently washed several times with water. The final residue was used for counting, after vacuum filtering through a nitrocellulose membrane (White SM/WP 5 μm, 19 mm, Millipore, Milan, Italy), using a phase contrast optical microscope (40×). Counts are reported as number of bodies per gram of dry tissue. The counts for the two tissues in this study ranged from 10×10^3 to 400×10^3 bodies per gram (dry tissue).

Histological examination and Perls' staining. For the histological analysis 3–5 μm sections of the paraffin-embedded lung tissue were mounted on glass slices and air-dried. Samples were deparaffinized and then stained with hematoxylin and eosin according to the standard procedure, or using Perls' staining. This is characterized by a potassium ferrocyanide solution, followed by a counterstaining with neutral red. Finally, samples were analysed using a Leica Microscope (LeicaMicrosystems GmbH, Germany). Chemicals were purchased from Sigma-Aldrich.

X-ray micro-spectroscopy at ID21. The XRF and XANES analyses using harder X-rays were carried out at the ID 21 beamline at the European Synchrotron Radiation Facility (ESRF, Grenoble, France), with the setup previously described[44,45]. The rejection of unwanted beam harmonics was ensured by a Ni coated silicon double mirror deflecting in the horizontal plane. A Si(111) fixed exit double crystal monochromator (Kohzu, Japan) was used to select and scan the beam energy. The 7.3 keV monochromatic X-ray beam was focused onto the sample using a Fresnel zone plate (Zone Plate Ltd, UK). The spot size was 0.2 μm × 1 μm with a photon flux of 3.5×10^9 photon/s/Si(111) band width. The sample was mounted on a custom x-y-z stage, tilted by 30° from the optical axis, facing a fluorescence detector placed 3.5 cm from the sample. This detector was a silicon drift diode (Bruker, Germany) with 80 mm^2 active surface equipped with a low energy polymer window. The incident beam intensity was monitored upstream of the sample using a drilled photodiode collecting the fluorescence signal from a thin Ti coated Si_3N_4 membrane inserted in the beam path. A transmission silicon photodiode was placed downstream of the sample and allowed the collection of absorption images, whilst simultaneously collecting the fluorescence signal. Images were acquired by raster scanning the samples under the beam, with a step size from 0.25 to 0.5 μm. The acquisition time was typically 300 ms/pixel. Deconvolution of the fluorescence elemental maps was performed using PyMCA software[32].

For micro-XANES measurements, the X-ray beam energy was scanned between 7.08 and 7.3 keV with 0.2 eV energy steps. Each XANES spectrum was acquired as the sum of ten quick scans with 100 ms integration time per point, for a total integration time of 1 s per point, to monitor possible photo-reduction effects linked to the beam. No modification of the XANES spectra with exposure time was observed. Energy calibration was performed using a Fe metal foil, whose K-edge was found at 7125.1 eV. XANES spectra of reference compounds (ferritin, haematite, magnetite, crocidolite fibres and fayalite) were collected to allow identification of the phases present in the sample by linear combination fitting. The spectra were base line subtracted and normalized to unity prior to fitting.

Soft X-ray microscopy and XRF at TwinMic. The absorption and differential phase contrast images and the XRF maps were acquired at the TwinMic beamline at the Elettra synchrotron facility in Trieste (Italy). The TwinMic station was operated in scanning X-ray microscopy mode (SXM)[46,47] where the beam is focused on the sample by zone plate diffractive optics providing sub-micron spatial resolution. The X-ray absorption and phase contrast images outline the morphological features of the sample at sub-micrometer length scales, whereas the simultaneous acquisition of the XRF maps[48,49] correlates the elemental distribution to the morphology. For the present experiments we selected X-ray energies to excite and get optimal emission conditions for the elements of major interest, namely Fe, Si and Mg and other lighter elements, in particular O, relevant to the formation mechanisms of the asbestos body. The images were acquired by raster-scanning the samples across the beam, with a spot size ranging from of 100 to 500 nm. The LEXRF dwell time varied between 2 and 20 seconds. The sample was mounted on an x-y-z stage (with the incoming beam perpendicular to the sample surface) facing 8 Silicon Drift Detectors placed 2 cm from the sample, with a total active area of 240 mm^2 [31].

The elemental distribution was obtained by processing and deconvoluting the XRF spectra with the PyMCA software[32].

1. Brims, F. J. Asbestos--a legacy and a persistent problem. *J. R. Nav. Med. Serv.* **95**, 4–11 (2009).
2. Straif, K. *et al.* A review of human carcinogens--part C: metals, arsenic, dusts, and fibres. *Lancet Oncol* **10**, 453–454 (2009).
3. Yang, H., Testa, J. R. & Carbone, M. Mesothelioma epidemiology, carcinogenesis, and pathogenesis. *Curr. Treat. Options. Oncol* **9**, 147–157 (2008).
4. Comar, M. *et al.* SV40 multiple tissue infection and asbestos exposure in a hyperendemic area for malignant mesothelioma. *Cancer Res* **67**, 8456–8459 (2007).
5. Ghio, A. J., Churg, A. & Roggli, V. L. Ferruginous bodies: implications in the mechanism of fiber and particle toxicity. *Toxicol. Pathol.* **32**, 643–649 (2004).
6. Zucali, P. A. *et al.* Advances in the biology of malignant pleural mesothelioma. *Cancer Treat. Rev* **37**, 543–558 (2011).
7. Kamp, D. W. Asbestos-induced lung diseases: an update. *Transl. Res* **153**, 143–152 (2009).
8. Donaldson, K., Murphy, F. A., Duffin, R. & Poland, C. A. Asbestos, carbon nanotubes and the pleural mesothelium: a review of the hypothesis regarding the role of long fibre retention in the parietal pleura, inflammation and mesothelioma. *Part Fibre. Toxicol.* **7**, 5 (2010).
9. Fenoglio, I. *et al.* Thickness of multiwalled carbon nanotubes affects their lung toxicity. *Chem. Res Toxicol.* **25**, 74–82 (2012).
10. Fenoglio, I., Fubini, B., Ghibaudi, E. M. & Turci, F. Multiple aspects of the interaction of biomacromolecules with inorganic surfaces. *Adv. Drug Deliv. Rev* **63**, 1186–1209 (2011).
11. Fubini, B. & Mollo, L. Role of iron in the reactivity of mineral fibers. *Toxicol. Lett* **82–83**, 951–960 (1995).
12. Fenoglio, I., Prandi, L., Tomatis, M. & Fubini, B. Free radical generation in the toxicity of inhaled mineral particles: the role of iron speciation at the surface of asbestos and silica. *Redox. Rep.* **6**, 235–241 (2001).
13. Turci, F., Tomatis, M., Lesci, I. G., Roveri, N. & Fubini, B. The Iron-Related Molecular Toxicity Mechanism of Synthetic Asbestos Nanofibres: A Model Study for High-Aspect-Ratio Nanoparticles. *Chemistry.* (2010).
14. Fubini, B., Barcelo, F. & Otero, A. C. Ferritin adsorption on amosite fibers: possible implications in the formation and toxicity of asbestos bodies. *J. Toxicol. Environ. Health* **52**, 343–352 (1997).
15. Ghio, A. J., Stonehuerner, J., Richards, J. & Devlin, R. B. Iron homeostasis in the lung following asbestos exposure. *Antioxid. Redox. Signal.* **10**, 371–377 (2008).
16. Dodson, R. F., Hammar, S. P. & Poye, L. W. A technical comparison of evaluating asbestos concentration by phase-contrast microscopy (PCM), scanning electron microscopy (SEM), and analytical transmission electron microscopy (ATEM) as illustrated from data generated from a case report. *Inhal. Toxicol.* **20**, 723–732 (2008).
17. Dodson, R. F. *et al.* A comparison of the ferruginous body and uncoated fiber content in the lungs of former asbestos workers. *Am. Rev. Respir. Dis.* **132**, 143–147 (1985).
18. Kell, D. B. Iron behaving badly: inappropriate iron chelation as a major contributor to the aetiology of vascular and other progressive inflammatory and degenerative diseases. *BMC. Med. Genomics* **2**, 2 (2009).
19. Kell, D. B. Towards a unifying, systems biology understanding of large-scale cellular death and destruction caused by poorly liganded iron: Parkinson's, Huntington's, Alzheimer's, prions, bactericides, chemical toxicology and others as examples. *Arch. Toxicol.* **84**, 825–889 (2010).
20. Ghio, A., Tan, R. J., Ghio, K., Fattman, C. L. & Oury, T. D. Iron accumulation and expression of iron-related proteins following murine exposure to crocidolite. *J. Environ. Pathol. Toxicol. Oncol.* **28**, 153–162 (2009).
21. Wang, X. *et al.* Iron uptake and Nramp2/DMT1/DCT1 in human bronchial epithelial cells. *Am. J. Physiol Lung Cell Mol. Physiol* **282**, L987–L995 (2002).
22. Yang, F. *et al.* Apical location of ferroportin 1 in airway epithelia and its role in iron detoxification in the lung. *Am. J. Physiol Lung Cell Mol. Physiol* **289**, L14–L23 (2005).
23. Dorger, M. & Krombach, F. Interaction of alveolar macrophages with inhaled mineral particulates. *J. Aerosol Med.* **13**, 369–380 (2000).
24. Goldsmith, C. A., Frevert, C., Imrich, A., Sioutas, C. & Kobzik, L. Alveolar macrophage interaction with air pollution particulates. *Environ. Health Perspect.* **105 Suppl 5**, 1191–1195 (1997).
25. Frazier, M. D., Mamo, L. B., Ghio, A. J. & Turi, J. L. Hepcidin expression in human airway epithelial cells is regulated by interferon-gamma. *Respir. Res* **12**, 100 (2011).
26. Nakamura, H. *et al.* Priming of alveolar macrophages for interleukin-8 production in patients with idiopathic pulmonary fibrosis. *Am. J. Respir. Crit Care Med.* **152**, 1579–1586 (1995).
27. Ortega, R., Deves, G. & Carmona, A. Bio-metals imaging and speciation in cells using proton and synchrotron radiation X-ray microspectroscopy. *J. R. Soc. Interface* **6 Suppl 5**, S649–S658 (2009).
28. Fahrni, C. J. Biological applications of X-ray fluorescence microscopy: exploring the subcellular topography and speciation of transition metals. *Curr. Opin. Chem. Biol.* **11**, 121–127 (2007).
29. Pascolo, L. *et al.* Synchrotron soft X-ray imaging and fluorescence microscopy reveal novel features of asbestos body morphology and composition in human lung tissues. *Part Fibre. Toxicol.* **8**, 7 (2011).
30. Tuomi, T. Fibrous minerals in the lungs of mesothelioma patients: comparison between data on SEM, TEM, and personal interview information. *Am. J. Ind. Med.* **21**, 155–162 (1992).
31. Roggli, V. L. The role of analytical SEM in the determination of causation in malignant mesothelioma. *Ultrastruct. Pathol.* **30**, 31–35 (2006).
32. Sole, A., Papillon, E., Cotte, M., Walter, P. & Susini, J. A multiplatform code for the analysis of energy-dispersive X-ray fluorescence spectra. *Spectrochim Acta B* **62**, 63–68 (2007).
33. Nakamura, E., Makishima, A., Hagino, K. & Okabe, K. Accumulation of radium in ferruginous protein bodies formed in lung tissue: association of resulting radiation hotspots with malignant mesothelioma and other malignancies. *Proc. Jpn. Acad. Ser. B Phys. Biol. Sci.* **85**, 229–239 (2009).
34. Bussy, C. *et al.* Carbon nanotubes in macrophages: imaging and chemical analysis by X-ray fluorescence microscopy. *Nano. Lett* **8**, 2659–2663 (2008).
35. Shimizu, Y. *et al.* Elemental analysis of lung tissue particles and intracellular iron content of alveolar macrophages in pulmonary alveolar proteinosis. *Respir. Res* **12**, 88 (2011).
36. Shimizu, Y. *et al.* In-air micro-particle induced X-ray emission analysis of asbestos and metals in lung tissue. *Int. J. Immunopathol. Pharmacol.* **21**, 567–576 (2008).
37. Quintana, C. Contribution of analytical microscopies to human neurodegenerative diseases research (PSP and AD). *Mini. Rev. Med. Chem.* **7**, 961–975 (2007).
38. Rinaudo, C. *et al.* Study of inorganic particles, fibers, and asbestos bodies by variable pressure scanning electron microscopy with annexed energy dispersive spectroscopy and micro-Raman spectroscopy in thin sections of lung and pleural plaque. *Appl Spectrosc.* **64**, 571–577 (2010).
39. Gutierrez, L. *et al.* Bioinorganic transformations of liver iron deposits observed by tissue magnetic characterisation in a rat model. *J. Inorg. Biochem.* **100**, 1790–1799 (2006).
40. Gutierrez, L. *et al.* Iron speciation study in Hfe knockout mice tissues: magnetic and ultrastructural characterisation. *Biochim. Biophys. Acta* **1792**, 541–547 (2009).
41. Michel, F. M. *et al.* Ordered ferrimagnetic form of ferrihydrite reveals links among structure, composition, and magnetism. *Proc. Natl. Acad. Sci. U. S. A* **107**, 2787–2792 (2010).
42. Asbestos, asbestosis, and cancer: the Helsinki criteria for diagnosis and attribution. *Scand. J. Work Environ. Health* **23**, 311–316 (1997).
43. Roggli, V. L., McGavran, M. H., Subach, J., Sybers, H. D. & Greenberg, S. D. Pulmonary asbestos body counts and electron probe analysis of asbestos body cores in patients with mesothelioma: a study of 25 cases. *Cancer* **50**, 2423–2432 (1982).
44. Bohic, S. *et al.* Biomedical applications of the ESRF synchrotron-based microspectroscopy platform. *J. Struct. Biol.* **177**, 248–258 (2012).
45. Delfino, R. *et al.* X-ray fluorescence elemental mapping and microscopy to follow hepatic disposition of a Gd-based magnetic resonance imaging contrast agent. *Clin. Exp. Pharmacol. Physiol* **38**, 834–845 (2011).
46. Gianoncelli, A. *et al.* Simultaneous Soft X-ray Transmission and Emission Microscopy. *Nuclear Instruments and Methods in Physics Research A* **608**, 195–198 (2009).
47. Kaulich, B. *et al.* Low-energy X-ray fluorescence microscopy opening new opportunities for bio-related research. *J. R. Soc. Interface* **6 Suppl 5**, S641–S647 (2009).
48. Gianoncelli, A., Morrison, G. R., Kaulich, B., Bacescu, D. & Kovac, J. A fast read-out CCD camera system for scanning X-ray microscopy. *Appl. Phys. Lett* **89**, 251117–251119 (2006).
49. Morrison, G. R., Gianoncelli, A., Kaulich, B., Bacescu, D. & Kovac, J. A fast read-out CCD system for configured-detector imaging in STXM. *Conf.Proc.Series IPAP* **7**, 277–379 (2006).

Acknowledgements

The authors acknowledge two grants from Friuli Venezia Giulia Region: Nanotox 0060 - 2009; and Commissione Amianto FVG -2011. We thank dr.Kevin Prince for careful reading of the manuscript.

Author contributions

LP designed and coordinated the study, was substantially involved in acquisition, analysis and interpretation of results, and drafted the manuscript. AG was substantially involved in data acquisition at TwinMic and analyses and revised the manuscript regarding the methodological aspects. GS was involved in sample preparation, histological experiments and data analyses, and she revised the manuscript. M Salomé was substantially involved in data acquisition at ID21, supervised data analyses and was responsible for XANES experiments, contributing to the manuscript. M Schneider was involved in human sample selection and diagnosis. CC contributed to the technical aspects of treatment of human samples and was responsible for staining procedures. MK actively contributed to data interpretation and critical and thorough revision of the manuscript. CR directed the work, coordinating the clinical aspects of the study. CR and MM, as experts in diagnosis of asbestos-related diseases, provided the cogent interpretation of the study and revised the manuscript. All authors have read and approved the final manuscript.

Additional information

Supplementary information accompanies this paper at http://www.nature.com/scientificreports

Competing financial interests: The authors declare no competing financial interests.

License: This work is licensed under a Creative Commons Attribution-NonCommercial-NoDerivs 3.0 Unported License. To view a copy of this license, visit http://creativecommons.org/licenses/by-nc-nd/3.0/

How to cite this article: Pascolo, L. *et al*. The interaction of asbestos and iron in lung tissue revealed by synchrotron-based scanning X-ray microscopy. *Sci. Rep.* **3**, 1123; DOI:10.1038/srep01123 (2013).